Geophys. J. Int. (2006) **165,** 641–657 doi: 10.1111/j.1365-246X.2006.02982.x

Finite-frequency vectorial tomography: a new method for high-resolution imaging of upper mantle anisotropy

Sébastien Chevrot

Laboratoire de Dynamique Terrestre et Planétaire, CNRS, UMR 5562, *Observatoire Midi-Pyrénées, Université Paul Sabatier, Toulouse III, France.*
E-mail: chevrot@dtp.obs-mip.fr

Accepted 2006 February 21. Received 2006 February 21; in original form 2005 September 28

SUMMARY

Amplitude measurements of the transverse component of *SKS* waves, the so-called splitting intensity, can be used to formulate a non-linear inverse problem to image the 3-D variations of upper mantle anisotropy. Assuming transverse isotropy (or hexagonal symmetry), one can parametrize anisotropy by two anisotropic parameters and two angles describing the orientation of the symmetry axis. These can also be written as two collinear pseudo-vectors. The tomographic process consists of retrieving the spatial distribution of these pseudo-vectors, and thus resembles surface wave vectorial tomography. Spatial resolution results from the sensitivity of low-frequency *SKS* waves to seismic anisotropy off the ray path. The expressions for the 3-D sensitivity kernels for splitting intensity are derived, including the near-field contributions, and validated by comparison with a full wave equation solution based upon the finite element method. These sensitivity kernels are valid for any orientation of the symmetry axis, and thus generalize previous results that were only valid for a horizontal symmetry axis. It is shown that both lateral and vertical subwavelength variations of anisotropy can be retrieved with a dense array of broad-band stations, even in the case of vertically propagating *SKS* waves.

Key words: Fréchet derivatives, scattering, seismic anisotropy, shear wave splitting, tomography.

1 INTRODUCTION

A few decades of seismological studies have shown that the upper mantle is anisotropic. This anisotropy is created primarily by the lattice preferred orientation of olivine, the most abundant mineral in the upper mantle. Seismic anisotropy can thus be used to infer mantle deformation and flow pattern.

While the large-scale anisotropic structures under the oceans seem to be related to seafloor spreading and present-day plate motion (e.g. Montagner & Tanimoto 1991), subcontinental anisotropy appears more complex, and is still poorly understood. For example, it is still unclear whether seismic anisotropy is produced by fossilized lithospheric fabrics (e.g. Silver 1996), by convective flow in the asthenosphere (e.g. Vinnik *et al.* 1992), or by a combination of both (e.g. Fouch *et al.* 2000). Distribution of seismic anisotropy under continents has also important implications regarding the mechanisms of lithospheric deformation. A first view is that the continental lithosphere behaves as a viscous fluid, with only the shallow crust deforming by faulting (e.g. Houseman & England 1986). The opposite view is that deformation is localized along major shear zones that reach the base of the lithosphere (e.g. Tapponnier *et al.* 1982).

Herquel *et al.* (1999) found evidence of strong variations of anisotropy along a profile crossing the Altyn Tagh fault. The strongest splitting near the fault was interpreted as localized deformation in the shear zone affecting the whole lithosphere. Strong, small-scale variations of anisotropy are also found in stable tectonic environments. For example, in the pre-Cambrian region of Kimberley, Fouch *et al.* (2004) found that the splitting decreases from 0.75 s in the NW of the Kimberley array to 0.15 s in the SE, over ∼50 km distance. To explain such extreme variations, they proposed a model composed of two blocks with distinct seismic anisotropy, separated by a sharp boundary. From this short overview of the problem, it is clear that a method capable of resolving lateral and vertical variations of seismic anisotropy over distances as short as a few tens of kilometres, well beyond the reach of surface wave tomography, would advance considerably our understanding of the deformation modes of the mantle. Such a method will be described here.

Inversions of teleseismic *P*-wave residuals in terms of both isotropic and anisotropic variations of phase velocity cannot resolve reliably lithospheric anisotropy, owing to poor distributions of rays in azimuth and incidence (Grésillaud & Cara 1996; Sobolev *et al.* 1999). In contrast, Vertical Seismic Profile experiments, which use distributions of sources and receivers in separate boreholes, usually offer an angular coverage that is sufficient for reliable anisotropic *P*-wave tomography (e.g. Pratt & Chapman 1992; Mensch & Farra 2002), but the depth penetration

of such experiments is only a few hundred metres. Using shear waves to image seismic anisotropy is even more difficult, because their phase velocity depends on both polarization and propagation directions. The problem is further complicated by the dependence of the polarization of the quasi-shear waves on the anisotropic properties of the medium (e.g. Jech & Pšenčík 1989). In contrast, the influence of isotropic heterogeneities on the time delay between the two quasi-shear waves is small (Červený & Simoes-Filho 1991). This interesting property can be exploited to map 3-D variations of seismic anisotropy from shear wave splitting measurements alone. Surprisingly, this opportunity has received little attention so far, mainly because it is widely believed that *SKS* waves have no vertical resolution, owing to their subvertical incidence.

When a shear wave crosses an anisotropic layer, it splits into two orthogonally polarized quasi-shear waves that propagate at different velocities. Two parameters are commonly used to describe the splitting, the time delay δt between the fast and the slow waves, and the polarization direction ϕ_0 of the fast wave. Because these two splitting parameters are rather easy to measure, they have been used extensively to infer average anisotropy under many broad-band stations (e.g. Silver 1996). Even with such a simple approach, it is sometimes difficult to characterize seismic anisotropy, because the apparent splitting parameters may vary as a function of azimuth of the incoming wave, which has heretofore been interpreted as evidence of vertical variations of anisotropy (e.g. Savage & Silver 1993). In addition, recent deployments of dense broad-band arrays have found evidence of significant lateral variations of the apparent splitting parameters over distances as short as a few tens of kilometres (e.g. Herquel *et al.* 1999; Fouch *et al.* 2004). These observations suggest that 3-D variations of seismic anisotropy map into apparent variations of the splitting parameters, and it seems natural to try to use them to image seismic anisotropy. However, the splitting parameters, which indeed capture average anisotropy under a station, are not so useful for a tomographic approach. The apparent polarization of the fast shear wave is biased towards the anisotropic properties close to the receiver (Červený & Simoes-Filho 1991, Saltzer *et al.* 2000). In addition, it is difficult to relate this parameter to perturbations of elastic parameters. The delay time may be more useful, as suggested by Červený & Simoes-Filho (1991), because it is not sensitive to isotropic heterogeneities along the wave path. However, the delay time is not measurable for polarizations close to the singular directions, which are parallel and perpendicular to the symmetry axis in a transversely isotropic medium. Since only a small subset of paths, corresponding to the strongest splittings, can be used, spatial coverage will be poor, resulting in coarse resolution.

For all these reasons, it seems necessary to define a new seismic observable to characterize shear wave splitting, that would be simply related to the elastic parameters and easy to measure: the amplitude of the transverse component of *SKS* waves. In an isotropic medium, shear waves are linearly polarized. Their polarization direction depends on the focal mechanism for *S* waves, and on the backazimuth of the source for *SKS* waves, which are polarized as *SV* after propagating through the liquid outer core. Should the *SKS* wave cross an anisotropic region along its upgoing leg, some energy will transfer to the transverse component, which would be zero otherwise. The transverse component of *SKS* waves can thus be seen as a perturbation of displacement produced by anisotropic perturbations of the elastic parameters. In the case of weak anisotropy, this displacement perturbation is obtained from the Born approximation and used to derive the 3-D sensitivity kernels for the transverse component amplitude, the so-called splitting intensity (Chevrot 2000; Favier & Chevrot 2003; Favier *et al.* 2004; Chevrot *et al.* 2004).

Hexagonal symmetry usually dominates the anisotropic part of the stiffness tensor of mantle rocks (Browaeys & Chevrot 2004). It is also the most simple type of anisotropic medium, described by only five elastic parameters and two angles that define the orientation of the symmetry axis. Assuming weak anisotropy, we can use the Born approximation to derive the perturbed transverse component of displacement. To describe shear wave splitting, we will show that only two anisotropic parameters and two angles are necessary, defining two pseudo-vectors. The inverse problem then consists in retrieving the spatial distribution of these pseudo-vectors, hence the name 'vectorial tomography'. A similar problem has been formulated by Montagner & Nataf (1988) with surface waves. In this approach, the orientation of the symmetry axis appears directly as a model parameter, which makes the introduction of *a priori* information on anisotropic fabrics straightforward.

The paper is organized as follows. After introducing the definition of splitting intensity, the perturbed displacement of shear waves in a weakly transversely isotropic medium is derived using the Born approximation. The Fréchet kernels of splitting intensity are then expressed as a function of perturbations of the elastic parameters and orientation of the symmetry axis. After describing the resolution of this inverse problem of a new kind, the method is applied to a synthetic example.

2 THE TRANSVERSE COMPONENT AMPLITUDE OF *SKS* WAVES

When required, we will use the following definitions of the Fourier transforms:

$$f(\omega) = \int_{-\infty}^{+\infty} f(t) e^{-i\omega t}\, dt, \tag{1}$$

$$f(t) = \frac{1}{2\pi} \int_{-\infty}^{+\infty} f(\omega) e^{i\omega t}\, d\omega. \tag{2}$$

Let us consider a radially polarized *SKS* wave propagating in an anisotropic medium. Arriving at the bottom of the anisotropic layer, the wave splits into a fast and a slow shear wave. Introducing $u_R^0(t)$ the incident wavelet, and β, the angle between the projection of the fast wave polarization in the horizontal plane and the radial direction, we can write the signals on the radial and transverse components recorded at the

surface as (Chevrot 2000):

$$u_R(t) = u_R^0(t + \delta t/2)\cos^2\beta + u_R^0(t - \delta t/2)\sin^2\beta, \tag{3}$$

$$\delta u_T(t) = -\frac{1}{2}\left[u_R^0(t + \delta t/2) - u_R^0(t - \delta t/2)\right]\sin 2\beta. \tag{4}$$

For a delay time that is small compared to the dominant period of the propagating wave, these expressions simplify to:

$$u_R(t) = u_R^0(t), \tag{5}$$

$$\delta u_T(t) = -\frac{1}{2}\,(\delta t \sin 2\beta)\,\dot{u}_R^0(t). \tag{6}$$

Note that at this point no assumption has been made regarding the symmetry and heterogeneity of the anisotropic medium. Thus, eqs (5) and (6) remain valid in a heterogeneous anisotropic medium. The transverse component is the time derivative of the radial component multiplied by a scalar, defined as the splitting intensity, and which mainly measures the amplitude of the transverse component.

The splitting intensity can thus be determined by projecting the transverse component on the derivative of the radial component:

$$S = 2\frac{Re\int i\omega\,\delta u_T(\omega)\,u_R^0(\omega)\,d\omega}{\int \omega^2|u_R^0(\omega)|^2\,d\omega}. \tag{7}$$

The similarity of (eq. 7) with the definition of the traveltime delay given by Dahlen *et al.* (2000)

$$\delta T = \frac{Re\int i\omega\,\delta u(\omega)\,u^0(\omega)\,d\omega}{\int \omega^2|u^0(\omega)|^2\,d\omega}, \tag{8}$$

where u^0 is the displacement in the reference isotropic medium and δu the perturbed displacement, suggests that the sensitivity kernels for splitting intensity can be derived in a similar way as the Fréchet derivatives of *P* and *S* traveltimes.

3 SCATTERING OF SHEAR WAVES IN TRANSVERSELY ISOTROPIC MEDIA

3.1 Born approximation in transversely isotropic media

To first order, the perturbations of displacement produced by small perturbations of the elastic parameters are given by (Hudson 1977):

$$\delta\mathbf{u}(\mathbf{r}) = \omega^2\int_V \delta\rho(\mathbf{x})\mathbf{G}^0(\mathbf{x},\mathbf{r})\mathbf{u}^0(\mathbf{x})\,d^3\mathbf{x} - \int_V [\delta\mathbf{c}(\mathbf{x}) : \mathbf{E}^0(\mathbf{x})] : [\nabla\mathbf{G}^0(\mathbf{x},\mathbf{r})]\,d^3\mathbf{x}, \tag{9}$$

where $\mathbf{G}^0$ is the Green's tensor, $\mathbf{u}^0$ the displacement, and $\mathbf{E}^0$ the strain tensor at location $\mathbf{x}$ in the reference medium. We consider an incident plane wave, that is, we neglect the curvature of the wave front, which is a good approximation owing to the rather small size of Fresnel zones of *SKS* waves in the upper mantle. Favier *et al.* (2004) have shown that near- and middle-field contributions to shear wave splitting are significant and must be taken into account. Thus, we need to consider the complete Green's tensor to compute the scattered wave field. The reference isotropic medium is assumed to be homogenous and infinite (the near-field contributions of reflections and conversions from the free surface are neglected), which simplifies the computation of the sensitivity kernels. Assuming a homogeneous reference isotropic model is equivalent to neglecting ray curvature of *SKS* in the outer 200 km of the upper mantle, which is indeed small when rays are traced in most reference earth models. The good agreement with the results of full waveform modelling shown below (see Section 5) shows that these different assumptions made in the computation of sensitivity kernels are reasonable.

The first term inside the brackets in eq. 9 defines a second-order moment tensor representing the sources of excitations produced by the volumetric distribution of anisotropic heterogeneities. Let us define this moment tensor by:

$$\mathbf{M}(\mathbf{x}) = \delta\mathbf{c}(\mathbf{x}) : \mathbf{E^0}(\mathbf{x}), \tag{10}$$

where the fourth-order tensor $\boldsymbol{\delta}\mathbf{c}$ represents the transversely isotropic perturbation of the stiffness tensor with respect to the isotropic reference medium:

$$\delta\mathbf{c} = \mathbf{c}^{\mathbf{TI}} - \mathbf{c}^{\mathbf{ISO}}, \tag{11}$$

$\mathbf{M}$ is symmetric, because of the symmetry of the fourth-order tensor $\boldsymbol{\delta}\mathbf{c}$.

A tensor can be defined without reference to any coordinate system (Backus 1970; Helbig 1994; Gangi 2000). The coordinate-free representations of stiffness tensors simplify the derivation of scattering coefficients considerably. Using the coordinate-free representations of the isotropic and transversely isotropic stiffness tensors given in Appendix A, $\boldsymbol{\delta}\mathbf{c}$ can be written in the form:

$$\begin{aligned}\delta c_{ijkl} = {} & (C_{11} - 2C_{66} - \lambda)\delta_{ij}\delta_{kl} + (C_{66} - \mu)(\delta_{ik}\delta_{jl} + \delta_{il}\delta_{jk}) \\ & + (C_{13} - C_{11} + 2C_{66})(\delta_{ij}s_k s_l + \delta_{kl}s_i s_j) \\ & + (C_{44} - C_{66})(\delta_{ik}s_j s_l + \delta_{il}s_j s_k + \delta_{jk}s_i s_l + \delta_{jl}s_i s_k) \\ & + (C_{11} + C_{33} - 2C_{13} - 4C_{44})s_i s_j s_k s_l\end{aligned} \tag{12}$$

where the unit vector $\hat{\mathbf{s}}$ represents the orientation of the symmetry axis. The choice of the reference isotropic medium is arbitrary as long as $\|\delta\mathbf{c}\| \ll \|\mathbf{c}^{\mathrm{ISO}}\|$. The P- and S-wave velocities in the reference medium are defined respectively as $\alpha = \sqrt{(\lambda + 2\mu)/\rho}$ and $\beta = \sqrt{\mu/\rho}$, where λ and μ are the Lamé parameters, and ρ the density. Introducing the dimensionless anisotropic parameters $\epsilon = (C_{11} - C_{33})/2\rho\alpha^2$, $\gamma = (C_{66} - C_{44})/2\rho\beta^2$ and $\delta = (C_{13} - C_{33} + 2C_{44})/\rho\alpha^2$ (Mensch & Rasolofosaon 1997), and the perturbations of the Lamé parameters $\delta\lambda = C_{11} - 2C_{66} - \lambda$ and $\delta\mu = C_{66} - \mu$, one can rewrite eq. (12) as:

$$\begin{aligned}\delta c_{ijkl} &= \delta\lambda\,\delta_{ij}\delta_{kl} + \delta\mu\,(\delta_{ik}\delta_{jl} + \delta_{il}\delta_{jk}) \\ &\quad + 2\rho\alpha^2\epsilon\,(s_i s_j s_k s_l - \delta_{ij}s_k s_l - \delta_{kl}s_i s_j) \\ &\quad + \rho\alpha^2\delta\,(\delta_{ij}s_k s_l + \delta_{kl}s_i s_j - 2s_i s_j s_k s_l) \\ &\quad + 2\rho\beta^2\gamma\,(2\delta_{ij}s_k s_l + 2\delta_{kl}s_i s_j - \delta_{ik}s_j s_l - \delta_{il}s_j s_k - \delta_{jk}s_i s_l - \delta_{jl}s_i s_k)\end{aligned} \tag{13}$$

Note that this definition of the perturbations of the Lamé parameters is the only one that limits the contributions of the fourth-order isotropic tensors to the isotropic part of $\boldsymbol{\delta}\mathbf{c}$. Other definitions would introduce contributions of fourth-order isotropic tensors in the parts that depend on the anisotropic parameters ϵ, γ and δ, and thus introduce some correlation between the different parameters.

Using the relations between perturbations of the compressional and shear wave speeds and perturbations of the Lamé parameters

$$2\rho\alpha\,\delta\alpha = \delta\lambda + 2\delta\mu - \alpha^2\delta\rho, \tag{14}$$

$$2\rho\beta\,\delta\beta = \delta\mu - \beta^2\delta\rho, \tag{15}$$

and neglecting the contribution of density perturbations, one obtains

$$\begin{aligned}\delta c_{ijkl} &= 2\rho\alpha^2\left(\frac{\delta\alpha}{\alpha}\right)\delta_{ij}\delta_{kl} + 2\rho\beta^2\left(\frac{\delta\beta}{\beta}\right)(\delta_{ik}\delta_{jl} + \delta_{il}\delta_{jk} - 2\delta_{ij}\delta_{kl}) \\ &\quad + 2\rho\alpha^2\epsilon\,(s_i s_j s_k s_l - \delta_{ij}s_k s_l - \delta_{kl}s_i s_j) \\ &\quad + \rho\alpha^2\delta\,(\delta_{ij}s_k s_l + \delta_{kl}s_i s_j - 2s_i s_j s_k s_l) \\ &\quad + 2\rho\beta^2\gamma\,(2\delta_{ij}s_k s_l + 2\delta_{kl}s_i s_j - \delta_{ik}s_j s_l - \delta_{il}s_j s_k - \delta_{jk}s_i s_l - \delta_{jl}s_i s_k)\end{aligned} \tag{16}$$

In the remainder of this paper, the unit slowness vectors of the incoming and outgoing waves are denoted by $\hat{\mathbf{p}}'$ and $\hat{\mathbf{p}}$, respectively, and the polarization of the incoming and outgoing waves $\hat{\mathbf{g}}'$ and $\hat{\mathbf{g}}$, respectively. With these definitions, a unit incident plane wave may be written

$$\mathbf{u}^{\mathbf{0}}(\mathbf{x},\omega) = m(\omega)\hat{\mathbf{g}}' e^{i\omega T'}, \tag{17}$$

and the associated strain

$$\mathbf{E}^{\mathbf{0}}(\mathbf{x},\omega) = \frac{i\omega}{2c'} m(\omega)(\hat{\mathbf{p}}'\hat{\mathbf{g}}' + \hat{\mathbf{g}}'\hat{\mathbf{p}}')\,\exp(i\omega T'), \tag{18}$$

where $m(\omega)$ is the Fourier transform of the pulse, which propagates at the velocity c'.

Making use of the fourth-order elasticity tensor (eq. 16) and second-order strain tensor (eq. 18), the second-order tensor $\mathbf{M}$ reduces to:

$$\mathbf{M} = \frac{i\omega}{c'}\,\tilde{\mathbf{M}}\,m(\omega)\,\exp(i\omega T'), \tag{19}$$

where

$$\begin{aligned}\tilde{\mathbf{M}} &= 2\rho\alpha^2\left(\frac{\delta\alpha}{\alpha}\right)(\hat{\mathbf{p}}'\cdot\hat{\mathbf{g}}')\,\mathbf{I} \\ &\quad + 2\rho\beta^2\left(\frac{\delta\beta}{\beta}\right)\left[\hat{\mathbf{p}}'\hat{\mathbf{g}}' + \hat{\mathbf{g}}'\hat{\mathbf{p}}' - 2(\hat{\mathbf{p}}'\cdot\hat{\mathbf{g}}')\,\mathbf{I}\right] \\ &\quad + 2\rho\alpha^2\,\epsilon\,\left[(\hat{\mathbf{p}}'\cdot\hat{\mathbf{s}})(\hat{\mathbf{g}}'\cdot\hat{\mathbf{s}})(\hat{\mathbf{s}}\hat{\mathbf{s}} - \mathbf{I}) - (\hat{\mathbf{p}}'\cdot\hat{\mathbf{g}}')\,\hat{\mathbf{s}}\hat{\mathbf{s}}\right] \\ &\quad + \rho\alpha^2\,\delta\,[(\hat{\mathbf{p}}'\cdot\hat{\mathbf{s}})(\hat{\mathbf{g}}'\cdot\hat{\mathbf{s}})(\mathbf{I} - 2\hat{\mathbf{s}}\hat{\mathbf{s}}) + (\hat{\mathbf{p}}'\cdot\hat{\mathbf{g}}')\,\hat{\mathbf{s}}\hat{\mathbf{s}}] \\ &\quad + 2\rho\beta^2\,\gamma\,[2(\hat{\mathbf{p}}'\cdot\hat{\mathbf{s}})(\hat{\mathbf{g}}'\cdot\hat{\mathbf{s}})\mathbf{I} + 2(\hat{\mathbf{p}}'\cdot\hat{\mathbf{g}}')\,\hat{\mathbf{s}}\hat{\mathbf{s}} - (\hat{\mathbf{g}}'\cdot\hat{\mathbf{s}})(\hat{\mathbf{p}}'\hat{\mathbf{s}} + \hat{\mathbf{s}}\hat{\mathbf{p}}') - (\hat{\mathbf{p}}'\cdot\hat{\mathbf{s}})(\hat{\mathbf{g}}'\hat{\mathbf{s}} + \hat{\mathbf{s}}\hat{\mathbf{g}}')]\end{aligned} \tag{20}$$

The moment tensor in eq. (20) is valid for any type of wave interaction in a transversely isotropic medium. For an incident shear wave, $(\hat{\mathbf{p}}'\cdot\hat{\mathbf{g}}') = 0$, and

$$\begin{aligned}\tilde{\mathbf{M}} &= 2\rho\beta^2\left(\frac{\delta\beta}{\beta}\right)(\hat{\mathbf{p}}'\hat{\mathbf{g}}' + \hat{\mathbf{g}}'\hat{\mathbf{p}}') \\ &\quad + 2\rho\alpha^2\,\epsilon\,(\hat{\mathbf{p}}'\cdot\hat{\mathbf{s}})(\hat{\mathbf{g}}'\cdot\hat{\mathbf{s}})(\hat{\mathbf{s}}\hat{\mathbf{s}} - \mathbf{I}) \\ &\quad + \rho\alpha^2\,\delta\,(\hat{\mathbf{p}}'\cdot\hat{\mathbf{s}})(\hat{\mathbf{g}}'\cdot\hat{\mathbf{s}})(\mathbf{I} - 2\hat{\mathbf{s}}\hat{\mathbf{s}}) \\ &\quad + 2\rho\beta^2\,\gamma\,[2(\hat{\mathbf{p}}'\cdot\hat{\mathbf{s}})(\hat{\mathbf{g}}'\cdot\hat{\mathbf{s}})\mathbf{I} - (\hat{\mathbf{g}}'\cdot\hat{\mathbf{s}})(\hat{\mathbf{p}}'\hat{\mathbf{s}} + \hat{\mathbf{s}}\hat{\mathbf{p}}') - (\hat{\mathbf{p}}'\cdot\hat{\mathbf{s}})(\hat{\mathbf{g}}'\hat{\mathbf{s}} + \hat{\mathbf{s}}\hat{\mathbf{g}}')]\end{aligned} \tag{21}$$

In a reference unbounded homogeneous isotropic medium, the perturbed shear wavefield in eq. (9) is given by (Aki & Richards 1980):

$$\delta u_n(\mathbf{r},t) = \int_V \left[\frac{15p_np_pp_q - 3p_n\delta_{pq} - 3p_p\delta_{nq} - 3p_q\delta_{np}}{4\pi\rho r^4} \int_{r/\alpha}^{r/\beta} \tau\, M_{pq}(\mathbf{x}, t-\tau)\, d\tau \right.$$
$$- \frac{6p_np_pp_q - p_n\delta_{pq} - p_p\delta_{nq} - 2p_q\delta_{np}}{4\pi\rho\beta^2 r^2} M_{pq}(\mathbf{x}, t-r/\beta)$$
$$\left. - \frac{p_np_p - \delta_{np}}{4\pi\rho\beta^3 r} p_q \dot{M}_{pq}(\mathbf{x}, t-r/\beta) \right] d^3\mathbf{x} \tag{22}$$

where δ_{pq} is the Kronecker delta, defined to be 1 if $p = q$ and 0 if $p \neq q$, r the distance between the scattering point $\mathbf{x}$ and the receiver at $\mathbf{r}$, and $\hat{\mathbf{p}}$ the unit slowness vector pointing from the scattering point to the receiver. Integrating the first term by parts gives a term proportional to r^{-4}, which I will call the local field, and a term proportional to r^{-3}, which I will call the near field. The second and third terms, which are proportional to r^{-2}, represent the middle field for P and S waves, respectively. The fourth and fifth terms, which are proportional to r^{-1}, represent the far field for P and S waves, respectively. Although the far field usually accounts for the dominant part of seismic signals, all the terms in eq. (22) have significant contributions to shear wave splitting for depths as large as the dominant wavelength (Favier *et al.* 2004). At larger depth, the far field becomes dominant.

At this point, it is convenient to move to the frequency domain, in which eq. (22) is transformed to

$$\delta u_n(\mathbf{r},\omega) = \int_V \left[\frac{1}{\omega^2} \frac{15p_np_pp_q - 3p_n\delta_{pq} - 3p_p\delta_{nq} - 3p_q\delta_{np}}{4\pi\rho r^4}\, M_{pq}(\mathbf{x},\omega) e^{-i\omega r/\beta} \right.$$
$$- \frac{1}{i\omega} \frac{15p_np_pp_q - 3p_n\delta_{pq} - 3p_p\delta_{nq} - 3p_q\delta_{np}}{4\pi\rho\beta r^3} M_{pq}(\mathbf{x},\omega) e^{-i\omega r/\beta}$$
$$- \frac{6p_np_pp_q - p_n\delta_{pq} - p_p\delta_{nq} - 2p_q\delta_{np}}{4\pi\rho\beta^2 r^2} M_{pq}(\mathbf{x},\omega) e^{-i\omega r/\beta}$$
$$\left. - i\omega\, \frac{p_np_p - \delta_{np}}{4\pi\rho\beta^3 r} p_q M_{pq}(\mathbf{x},\omega) e^{-i\omega r/\beta} \right] d^3\mathbf{x} \tag{23}$$

The contribution of scattered P waves to shear wave splitting in the near field is very small (see Favier *et al.* 2004) and is thus neglected in eq. (23).

3.2 The transverse component of *SKS* waves

After passing through the outer core, *SKS* waves are polarized in the radial direction, that is, in the vertical plane containing the source and the receiver. If the mantle is isotropic and if *SKS* waves do not cross dipping interfaces, there should be no energy in the transverse component. However, if *SKS* waves encounter an anisotropic region during their propagation from the core-mantle boundary to the surface, they will split into two quasi-shear waves that are polarized orthogonally. Then, the perturbation of the transverse component of displacement is obtained by projecting the perturbed displacement on the transverse direction:

$$\delta u_t(\mathbf{r}) = \hat{\mathbf{t}} \cdot \delta\mathbf{u}(\mathbf{r}). \tag{24}$$

Introducing the second-order moment tensor (21) inside (9), and using the definition (24), we obtain:

$$\delta u_t(\mathbf{r},\omega) = \int_V \left[\frac{\beta}{i\omega} \frac{\left(\Omega_\beta^{LF}\left(\frac{\delta\beta}{\beta}\right) + \Omega_\epsilon^{LF}\epsilon + \Omega_\delta^{LF}\delta + \Omega_\gamma^{LF}\gamma\right)}{4\pi r^4} m(\omega)\ , \right. \tag{25}$$

$$+ \frac{\left(\Omega_\beta^{NF}\left(\frac{\delta\beta}{\beta}\right) + \Omega_\epsilon^{NF}\epsilon + \Omega_\delta^{NF}\delta + \Omega_\gamma^{NF}\gamma\right)}{4\pi r^3} m(\omega), \tag{26}$$

$$+ i\omega \frac{\left(\Omega_\beta^{MF}\left(\frac{\delta\beta}{\beta}\right) + \Omega_\epsilon^{MF}\epsilon + \Omega_\delta^{MF}\delta + \Omega_\gamma^{MF}\gamma\right)}{4\pi\beta r^2} m(\omega), \tag{27}$$

$$\left. + \omega^2 \frac{\left(\Omega_\beta^{FF}\left(\frac{\delta\beta}{\beta}\right) + \Omega_\epsilon^{FF}\epsilon + \Omega_\delta^{FF}\delta + \Omega_\gamma^{FF}\gamma\right)}{4\pi\beta^2 r} m(\omega) \right] d^3\mathbf{x}, \tag{28}$$

where the radial-to-transverse scattering coefficients are given by:

$$\Omega_\beta^{LF} = \Omega_\beta^{NF} = -60(\hat{\mathbf{p}}\cdot\hat{\mathbf{t}})(\hat{\mathbf{p}}\cdot\hat{\mathbf{p}}')(\hat{\mathbf{p}}\cdot\hat{\mathbf{g}}'), \tag{29}$$

$$\Omega_\epsilon^{LF} = \Omega_\epsilon^{NF} = \frac{\alpha^2}{\beta^2}(\hat{\mathbf{p}}'\cdot\hat{\mathbf{s}})(\hat{\mathbf{g}}'\cdot\hat{\mathbf{s}})\left[6(\hat{\mathbf{p}}\cdot\hat{\mathbf{t}}) - 30(\hat{\mathbf{p}}\cdot\hat{\mathbf{t}})(\hat{\mathbf{p}}\cdot\hat{\mathbf{s}})^2 + 12(\hat{\mathbf{p}}\cdot\hat{\mathbf{s}})(\hat{\mathbf{t}}\cdot\hat{\mathbf{s}})\right], \tag{30}$$

$$\Omega_\delta^{LF} = \Omega_\delta^{NF} = -\Omega_\epsilon^{LF}, \tag{31}$$

$$\Omega_{\gamma}^{LF} = \Omega_{\gamma}^{NF} = \left[(\hat{\mathbf{g}}' \cdot \hat{\mathbf{s}})(\hat{\mathbf{p}} \cdot \hat{\mathbf{p}}') + (\hat{\mathbf{p}}' \cdot \hat{\mathbf{s}})(\hat{\mathbf{p}} \cdot \hat{\mathbf{g}}')\right]\left[60(\hat{\mathbf{p}} \cdot \hat{\mathbf{t}})(\hat{\mathbf{p}} \cdot \hat{\mathbf{s}}) - 12(\hat{\mathbf{t}} \cdot \hat{\mathbf{s}})\right] - 24(\hat{\mathbf{p}} \cdot \hat{\mathbf{t}})(\hat{\mathbf{p}}' \cdot \hat{\mathbf{s}})(\hat{\mathbf{g}}' \cdot \hat{\mathbf{s}}) \tag{32}$$

$$\Omega_{\beta}^{MF} = -24(\hat{\mathbf{p}} \cdot \hat{\mathbf{t}})(\hat{\mathbf{p}} \cdot \hat{\mathbf{p}}')(\hat{\mathbf{p}} \cdot \hat{\mathbf{g}}'), \tag{33}$$

$$\Omega_{\epsilon}^{MF} = \frac{\alpha^2}{\beta^2}(\hat{\mathbf{p}}' \cdot \hat{\mathbf{s}})(\hat{\mathbf{g}}' \cdot \hat{\mathbf{s}})\left[2(\hat{\mathbf{p}} \cdot \hat{\mathbf{t}}) - 12(\hat{\mathbf{p}} \cdot \hat{\mathbf{t}})(\hat{\mathbf{p}} \cdot \hat{\mathbf{s}})^2 + 6(\hat{\mathbf{p}} \cdot \hat{\mathbf{s}})(\hat{\mathbf{t}} \cdot \hat{\mathbf{s}})\right], \tag{34}$$

$$\Omega_{\delta}^{MF} = -\Omega_{\epsilon}^{MF}, \tag{35}$$

$$\Omega_{\gamma}^{MF} = \left[(\hat{\mathbf{g}}' \cdot \hat{\mathbf{s}})(\hat{\mathbf{p}} \cdot \hat{\mathbf{p}}') + (\hat{\mathbf{p}}' \cdot \hat{\mathbf{s}})(\hat{\mathbf{p}} \cdot \hat{\mathbf{g}}')\right]\left[24(\hat{\mathbf{p}} \cdot \hat{\mathbf{t}})(\hat{\mathbf{p}} \cdot \hat{\mathbf{s}}) - 6(\hat{\mathbf{t}} \cdot \hat{\mathbf{s}})\right] - 8(\hat{\mathbf{p}} \cdot \hat{\mathbf{t}})(\hat{\mathbf{p}}' \cdot \hat{\mathbf{s}})(\hat{\mathbf{g}}' \cdot \hat{\mathbf{s}}) \tag{36}$$

$$\Omega_{\beta}^{FF} = -4(\hat{\mathbf{p}} \cdot \hat{\mathbf{t}})(\hat{\mathbf{p}} \cdot \hat{\mathbf{p}}')(\hat{\mathbf{p}} \cdot \hat{\mathbf{g}}'), \tag{37}$$

$$\Omega_{\epsilon}^{FF} = 2\frac{\alpha^2}{\beta^2}\left[(\hat{\mathbf{t}} \cdot \hat{\mathbf{s}}) - (\hat{\mathbf{p}} \cdot \hat{\mathbf{s}})(\hat{\mathbf{p}} \cdot \hat{\mathbf{t}})\right](\hat{\mathbf{p}} \cdot \hat{\mathbf{s}})(\hat{\mathbf{p}}' \cdot \hat{\mathbf{s}})(\hat{\mathbf{g}}' \cdot \hat{\mathbf{s}}), \tag{38}$$

$$\Omega_{\delta}^{FF} = -\Omega_{\epsilon}^{FF}, \tag{39}$$

$$\Omega_{\gamma}^{FF} = -2\left[(\hat{\mathbf{g}}' \cdot \hat{\mathbf{s}})(\hat{\mathbf{p}} \cdot \hat{\mathbf{p}}') + (\hat{\mathbf{p}}' \cdot \hat{\mathbf{s}})(\hat{\mathbf{p}} \cdot \hat{\mathbf{g}}')\right]\left[(\hat{\mathbf{t}} \cdot \hat{\mathbf{s}}) - 2(\hat{\mathbf{p}} \cdot \hat{\mathbf{s}})(\hat{\mathbf{p}} \cdot \hat{\mathbf{t}})\right]. \tag{40}$$

The coefficients related to the isotropic perturbations of β depend on the scalar products $(\hat{\mathbf{p}} \cdot \hat{\mathbf{t}})$ and $(\hat{\mathbf{p}} \cdot \hat{\mathbf{g}}')$. Both scalar products are zero in the forward direction, which implies that the contribution of isotropic heterogeneities to shear wave splitting is negligible. This gives a formal proof that shear wave splitting is insensitive to isotropic structures, as suggested in Červený & Simoes-Filho (1991). In the following, isotropic perturbations will thus be neglected.

Another interesting result is that the scattering coefficients for δ are the opposite of the scattering coefficients for ϵ. This means that only the difference $\epsilon - \delta$ can be resolved from shear wave splitting measurements, which suggests to introduce a new anisotropic parameter $\eta = \epsilon - \delta$. This parameter makes no contribution to the transverse component in the singular propagation directions. For example, its contribution is zero in the case of a wave propagating vertically through a medium with a horizontal symmetry axis. In the case of a dipping symmetry axis, the η terms contribute to the amplitude of the transverse component, even if the incidence angle is small, as is the case for *SKS* waves (see also Chevrot & van der Hilst 2003).

4 FRÉCHET DERIVATIVES OF SPLITTING INTENSITY

4.1 Fréchet derivatives with respect to the anisotropic parameters

Splitting intensity is defined by (Chevrot 2000):

$$S = -2\frac{\int \delta u_T(t)\dot{u}_R(t)\,dt}{\int \dot{u}_R^2(t)\,dt} = 2\frac{Re\int i\omega\delta u_T(\omega)u_R^*(\omega)\,d\omega}{\int \omega^2|u_R(\omega)|^2\,d\omega}. \tag{41}$$

Using the results of the previous section, we write the splitting intensity in the form:

$$S = \int [K_{\gamma}(\mathbf{x})\gamma(\mathbf{x}) + K_{\eta}(\mathbf{x})\eta(\mathbf{x})]\,d^3\mathbf{x}, \tag{42}$$

where K_{γ} and K_{η} are the Fréchet derivatives relating the splitting intensity to the anisotropic perturbations γ and η. In the case of weak anisotropy, expression (42) derived from first-order Born theory describes splitting intensity with great accuracy as will be show in Section 5.

Using the scattering coefficients derived in the previous section, we then find the kernels for the anisotropic parameters γ and η:

$$\begin{aligned} K_{\gamma,\eta}(\mathbf{x}) = {} & \frac{\beta}{2\pi r^4}\Omega_{\gamma,\eta}^{LF}(\mathbf{x})\frac{\int |m(\omega)|^2\cos\omega\Delta T\,d\omega}{\int \omega^2|m(\omega)|^2\,d\omega} \\ & + \frac{1}{2\pi r^3}\Omega_{\gamma,\eta}^{NF}(\mathbf{x})\frac{\int \omega|m(\omega)|^2\sin\omega\Delta T\,d\omega}{\int \omega^2|m(\omega)|^2\,d\omega} \\ & - \frac{1}{2\pi\beta r^2}\Omega_{\gamma,\eta}^{MF}(\mathbf{x})\frac{\int \omega^2|m(\omega)|^2\cos\omega\Delta T\,d\omega}{\int \omega^2|m(\omega)|^2\,d\omega} \\ & + \frac{1}{2\pi\beta^2 r}\Omega_{\gamma,\eta}^{FF}(\mathbf{x})\frac{\int \omega^3|m(\omega)|^2\sin\omega\Delta T\,d\omega}{\int \omega^2|m(\omega)|^2\,d\omega} \end{aligned} \tag{43}$$

where ΔT is the differential traveltime between the ray scattered at $\mathbf{x}$ and the reference ray. The relation (43) is valid for any propagating pulse. It can be greatly simplified by considering the case of a Ricker pulse, represented by the second derivative of a Gaussian, which is a

particularly good analogue of the radial component of *SKS* waves. The power spectrum of the pulse

$$|m(\omega)|^2 = \frac{\omega^4\tau^2}{4\pi}\exp\left(-\frac{\omega^2\tau^2}{8\pi^2}\right), \tag{44}$$

has a dominant period $\tau_d = \tau/2$. Upon substituting the power spectrum (44) into relation (43) and using the integration formula discussed in Appendix B, we obtain the analytical expressions of the Fréchet derivatives:

$$\begin{aligned} K_{\gamma,\eta}(\mathbf{x}) = {} & \frac{\beta\tau^2}{480\pi^3 r^4}\Omega^{LF}_{\gamma,\eta}(\mathbf{x})\exp\left(-\frac{a^2}{4b^2}\right)H_4\left(\frac{a}{2b}\right), \\ & + \frac{\tau}{240\sqrt{2}\pi^2 r^3}\Omega^{NF}_{\gamma,\eta}(\mathbf{x})\exp\left(-\frac{a^2}{4b^2}\right)H_5\left(\frac{a}{2b}\right), \\ & + \frac{1}{240\pi\beta r^2}\Omega^{MF}_{\gamma,\eta}(\mathbf{x})\exp\left(-\frac{a^2}{4b^2}\right)H_6\left(\frac{a}{2b}\right), \\ & - \frac{1}{120\sqrt{2}\beta^2\tau r}\Omega^{FF}_{\gamma,\eta}(\mathbf{x})\exp\left(-\frac{a^2}{4b^2}\right)H_7\left(\frac{a}{2b}\right), \end{aligned} \tag{45}$$

where $a = \Delta T$, $b^2 = \tau^2/8\pi^2$, and H_n are the nth-order Hermite polynomials. The Fréchet derivatives depend on the orientation of the symmetry axis (through the amplitude of the scattering coefficients), which makes the inverse problem non-linear if the orientation of the symmetry axis is not known *a priori*.

Expression (45) generalizes the formula obtained by Favier & Chevrot (2003) which were only valid for a horizontal symmetry axis.

4.2 Fréchet derivatives with respect to the orientation of the symmetry axis

To estimate all the anisotropic properties of the medium, we will also need the Fréchet derivatives with respect to θ, the inclination of the symmetry axis, and ϕ, the azimuth of the symmetry axis in the horizontal plane. These Fréchet derivatives are simply obtained by applying the chain rule to eq. (42):

$$\left(\frac{\partial S}{\partial\theta}\right) = \gamma\left(\frac{\partial K_\gamma}{\partial s_i}\right)\left(\frac{\partial s_i}{\partial\theta}\right) + \eta\left(\frac{\partial K_\eta}{\partial s_i}\right)\left(\frac{\partial s_i}{\partial\theta}\right), \tag{46}$$

$$\left(\frac{\partial S}{\partial\phi}\right) = \gamma\left(\frac{\partial K_\gamma}{\partial s_i}\right)\left(\frac{\partial s_i}{\partial\phi}\right) + \eta\left(\frac{\partial K_\eta}{\partial s_i}\right)\left(\frac{\partial s_i}{\partial\phi}\right). \tag{47}$$

5 COMPARISON WITH FULL WAVEFORM MODELLING

The validity of eq. (45) for a vertically propagating *SKS* wave and a symmetry axis lying in the horizontal plane has been investigated in Chevrot *et al.* (2004). This comparison is now generalized to the case of an oblique incidence and a general orientation of the symmetry axis in an inhomogeneous anisotropic medium. Synthetic seismograms are computed with a spectral element method (SEM), which is a highly accurate technique for modelling seismic wave propagation in elastic media (Komatitsch & Tromp 2002). The SEM can take into account the full anisotropic elastic tensor with 21 coefficients (Komatitsch *et al.* 2000). The propagation of a plane wave is simulated by introducing an initial Gaussian-shape analytical displacement and its corresponding velocity field in the explicit time marching scheme. To attenuate the edge effects, the contour integral of the traction on the edges of the box produced by the analytical source is subtracted at each time step. This leads to accurate synthetic seismograms in the centre of the box.

The test case consists of two homogeneous anisotropic blocks, with a fast axis direction at -20° azimuth in the left block and at 90° in the right block. Inside each block, $\gamma = -0.03$ and $\eta = 0$ between 40 and 160 km depth. The boundary between the two blocks corresponds to the plane $x = 0$.

The splitting intensity for a vertically propagating *SKS* wave measured on the synthetic seismograms recorded at the station located above the boundary between the two blocks is shown with black circles in Fig. 1. The dominant period of the Gaussian wavelet is 10 s. The variation of splitting intensity with azimuth is described by a sinusoid whose amplitude gives the delay δt and its phase the orientation of the symmetry axis (Chevrot 2000; Favier & Chevrot 2003). Integrating the product between γ and its Fréchet derivative over the whole volume gives the splitting intensity predicted by the sensitivity kernels, shown by the solid line. An excellent agreement is observed between the two types of calculations, demonstrating the potential of 3-D sensitivity kernels for describing splitting intensity in heterogeneous anisotropic media. However, the computation of splitting intensity based upon integration of sensitivity kernels is much faster and can be performed on a modest computer. The other stations also show a sinusoidal variation of splitting intensity as a function of backazimuth. The variations of the apparent splitting parameters δt and ϕ_0 along a profile perpendicular to the boundary between the two blocks are shown in Figs 2 and 3. Far from the boundary, the apparent splitting parameters are in agreement with the predictions of geometrical ray theory, and reflect the anisotropic properties of the underlying medium. However, a smooth transition is observed between these two regions, whose width increases

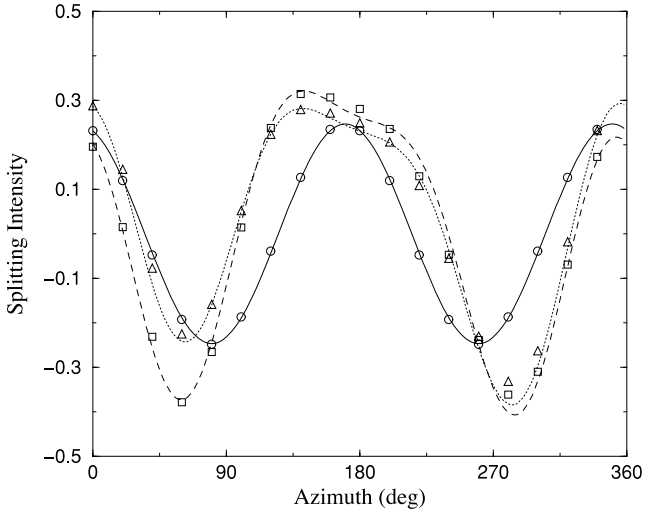

Figure 1. Splitting intensity for the station above the boundary between two anisotropic blocks. Inside each block, $\gamma = -0.03$ and $\eta = 0$ between 40 and 160 km depth. The azimuth of the symmetry axis is -20° in the left block and 90° in the right block. Splitting intensity is calculated by integrating sensitivity kernels, for a vertically propagating *SKS* wave (solid line) and for a 10° incidence angle (dashed line), compared to splitting intensity measured on the synthetic seismograms computed by SEM (circles and squares, respectively). The dominant period of the wave is 10 s. The last case corresponds to a dipping axis of symmetry: the angle from the vertical is 70° in the left block, and 110° in the right block. Splitting intensity calculated by integrating sensitivity kernels for an incidence angle of 10° is shown by the dotted line. Splitting intensity measured on the synthetic seismograms is shown by the triangles.

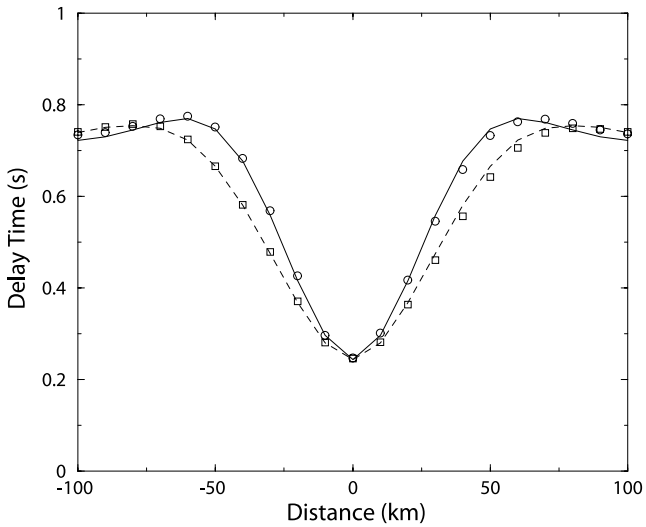

Figure 2. Apparent delay time observed along a linear profile for a vertically propagating *SKS* wave in the two block model. The predictions based upon integrating sensitivity kernels for a 10 s dominant period (solid line) and a 15 s dominant period (dashed line) are compared to the measurements made on synthetic seismograms computed by SEM (empty circles and squares).

with the dominant period of the wave. For a Gaussian waveform, it is about 100 km for a dominant period $\tau = 10$ s, and about 150 km for a dominant period $\tau = 15$ s. At the location of the boundary, the delay time drops by a factor 3. Thus, small-scale variations of anisotropy can produce small apparent anisotropy at the surface even if there is strong seismic anisotropy in the underlying medium (Chevrot *et al.* 2004).

For an oblique incidence, the variations of splitting intensity with polarization of the incident wave observed at stations close to the boundary are more complicated. Fig. 1 shows the splitting intensity at the station above the boundary for an incidence angle of 10°. In contrast to the vertical incidence case, splitting intensity is no longer described by a sinusoid. Any attempt to characterize seismic anisotropy with a delay time and a fast axis direction would be meaningless since these apparent parameters vary with azimuth. The problem is now truly 3-D. However, an almost perfect agreement is still observed between the measurements made on the synthetic seismograms and the kernel predictions. Even more complexity is observed for a dipping axis of symmetry, but the SEM and kernel computations are still found to be in good agreement. For example, Fig. 1 shows the splitting intensity at the same station as before, but for a symmetry axis at 70° from the vertical in the left block, and at 110° in the right block (dotted line and triangles).

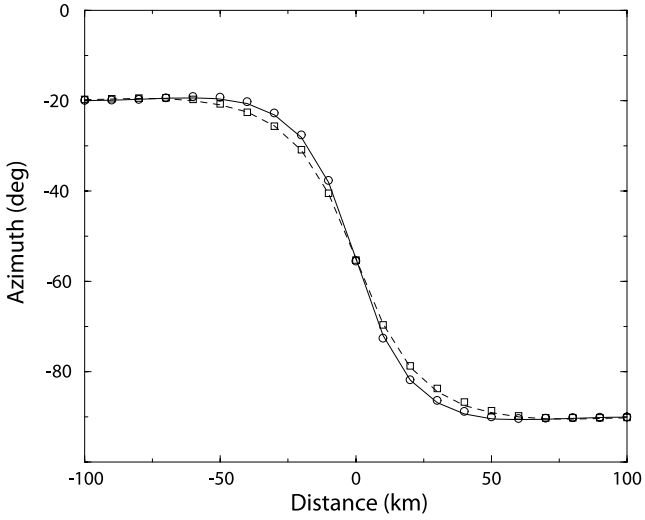

Figure 3. Apparent fast direction observed along a linear profile for a *SKS* wave propagating vertically in the two block model. The predictions based upon integrating sensitivity kernels for a 10 s dominant period (solid line) and a 15 s dominant period (dashed line) are compared to the measurements made on synthetic seismograms computed by SEM modelling (empty circles and squares).

The comparison between the results of full wave propagation and the sensitivity kernels shows that indeed the latter accurately describe shear wave splitting in 3-D anisotropic media. The sensitivity kernels offer a very efficient numerical scheme to solve the forward problem. In the following, after describing the method to solve the non-linear tomographic problem, we will test it in a synthetic numerical experiment.

6 INVERSION

The inverse problem consists of estimating the orientation of the symmetry axis and the parameters γ and η that best explain the observed *SKS* splitting in a least-squares sense.

6.1 Description of model parametrization

The precise depth distribution of seismic anisotropy is still an outstanding question but it is reasonable to assume that it is located in the top 200 km of the upper mantle. Thus, the model corresponds to the volume of the Earth under the array and in the depth interval between 200 km depth and the Moho, whose typical depth under continents is 40 km. The model is divided into cubic blocks of size smaller than the wavelength (about 1/10 of the Fresnel zone width at 100 km depth), to be able to resolve subwavelength anisotropic heterogeneities. A size of 10 km offers a good compromise between resolution and number of parameters. It is necessary to use a finer grid for the computation of the kernels (2 km blocks), for numerical accuracy. The Fréchet derivatives that are used in the inversion are computed in the fine grid and then integrated in the coarse grid. Inside each block, anisotropy is parametrized by γ and η, and two angles θ and ϕ which describe the local orientation of the symmetry axis.

6.2 The nature of *a priori* information

The set of anisotropy models that predict splitting measurements equally well is likely to be quite large. Including *a priori* information in the inversion constrains the range of admissible models. A model is represented by a vector $\mathbf{m}$ with Gaussian uncertainties described by the covariance operator $\mathbf{C}_{\mathrm{M}}$. The vector $\mathbf{m}_{\mathbf{prior}}$ represents the model constructed from the available information on the model before inversion. For example, we may have some *a priori* knowledge about the depth distribution of anisotropy, or about the amplitude of shear wave anisotropy, and use this information to define γ_{prior}. The *a priori* variance will allow us to define the range for admissible values of γ. If the *a priori* knowledge is weak, the variance will be large.

Using the decomposition described in Browaeys & Chevrot (2004), Becker *et al.* (2006) extracted the hexagonal part of the stiffness tensors of synthetic mantle fabrics, obtained by computing lattice preferred orientation of olivine and enstatite aggregates deformed by mantle flow, following the theory of Kaminski & Ribe (2001). They found that the anisotropic parameters ϵ, γ and δ are strongly correlated and that the fabrics of mantle xenoliths are well reproduced by numerical experiments. For $\epsilon \leq -0.03$, the anisotropic parameters are well described by the linear relations (Becker *et al.* 2006):

$$\gamma = -0.023 + 0.233\,\epsilon, \tag{48}$$

$$\delta = 0.027 + 1.857\,\epsilon. \tag{49}$$

Such *a priori* information is important, because it allows us to reduce the number of free parameters in the inversion. In order to characterize shear wave splitting, only one parameter is thus needed, say γ, instead of the two parameters γ and η.

While simple shear is probably the dominant mode of deformation in the upper mantle (Zhang & Karato 1995), uniaxial compression may be important in regions where the vertical component of mantle flow is dominant. These two modes of deformation produce very different types of fabrics. In simple shear deformation experiments, the lattice preferred orientation of olivine is aligned with the shear plane (Zhang *et al.* 2000), and the olivine aggregates possess a quasi-hexagonal symmetry, with a fast symmetry axis oriented along the shear direction. On the other hand, in uniaxial compression experiments, the *a* axis of olivine tends to fall randomly in the plane perpendicular to the shortening direction. This fabric is also quasi-hexagonal but the symmetry axis is slow and is oriented along the shortening direction. Simple shear is thus associated with a fast symmetry axis, described by negative γ, and uniaxial compression with a slow symmetry axis, described by positive γ. Given the *a priori* information on the mode of deformation of olivine, we can constrain the sign of γ.

We may also introduce some prior information on the orientation of the symmetry axis. For example, it is possible to impose an horizontal symmetry axis by assuming $\theta_{\text{prior}} = \pi/2$ with a very small *a priori* variance for this parameter.

Therefore, flexibility is an important aspect of the chosen model parametrization, which allows us to incorporate *a priori* assumptions on anisotropy in a straightforward way. If we chose instead to parametrize the problem in terms of perturbations of the stiffness tensor defined in a fixed Cartesian coordinate system, as in Pratt & Chapman (1992), such simple *a priori* information would be very difficult to include in the inversion.

6.3 The inverse problem

Defining $\mathbf{S}_{\text{obs}}$, the data vector containing the splitting intensity measurements, and $\mathbf{C}_{\text{S}}$ the covariance matrix containing their uncertainties, the maximum likelihood model minimizes the cost function (Tarantola 1987):

$$\chi(\mathbf{m}) = [\mathbf{S}(\mathbf{m}) - \mathbf{S}_{\text{obs}}]^t\, \mathbf{C}_{\text{S}}^{-1} [\mathbf{S}(\mathbf{m}) - \mathbf{S}_{\text{obs}}] + [\mathbf{m} - \mathbf{m}_{\text{prior}}]^t \mathbf{C}_{\text{M}}^{-1} [\mathbf{m} - \mathbf{m}_{\text{prior}}]. \tag{50}$$

Retrieving spatial variations of anisotropy involves too many parameters to systematically explore the model space. Instead, we solve the non-linear least-squares problem (50) by an iterative Gauss-Newton algorithm. Let $\mathbf{m}_n$ represent the current model at iteration n and $\mathbf{G}$ the matrix of partial (or Fréchet) derivatives of splitting intensity with respect to model parameters:

$$\mathbf{G} = \left(\frac{\partial \mathbf{S}}{\partial \mathbf{m}} \right)_{\mathbf{m}_n}. \tag{51}$$

At each iteration, the problem is linearized around the current model $\mathbf{m}_n$, and we search for the minimum of the misfit function

$$\begin{aligned} \chi(\boldsymbol{\Delta}\mathbf{m}) = {} & [\mathbf{S}(\mathbf{m}_n) + \mathbf{G}\boldsymbol{\Delta}\mathbf{m} - \mathbf{S}_{\text{obs}}]^t\, \mathbf{C}_{\text{S}}^{-1}\, [\mathbf{S}(\mathbf{m}_n) + \mathbf{G}\boldsymbol{\Delta}\mathbf{m} - \mathbf{S}_{\text{obs}}] \\ & + [\mathbf{m}_n + \boldsymbol{\Delta}\mathbf{m} - \mathbf{m}_{\text{prior}}]^t\, \mathbf{C}_{\text{M}}^{-1}\, [\mathbf{m}_n + \boldsymbol{\Delta}\mathbf{m} - \mathbf{m}_{\text{prior}}] \end{aligned} \tag{52}$$

where $\boldsymbol{\Delta}\,\mathbf{m}$ is the vector containing the parameter perturbations. By differentiating eq. (52) and setting the result to zero, we find that $\boldsymbol{\Delta}\mathbf{m}$ is a solution of the linear system

$$\left(\mathbf{G}^t \mathbf{C}_{\text{S}}^{-1} \mathbf{G} + \mathbf{C}_{\text{M}}^{-1}\right) \boldsymbol{\Delta}\mathbf{m} = \mathbf{G}^t \mathbf{C}_{\text{S}}^{-1} [\mathbf{S}_{\text{obs}} - \mathbf{S}(\mathbf{m}_n)] + \mathbf{C}_{\text{M}}^{-1} [\mathbf{m}_{\text{prior}} - \mathbf{m}_n]. \tag{53}$$

6.4 Regularization with smoothness constraints

In practice, it is necessary to regularize eq. (53) by incorporating smoothess constraints into the misfit function (52). The roughness penalty allows the smooth eigenvectors in the null space of the unconstrained problem to contribute to the solution (Scales *et al.* 1990; Ory & Pratt 1995). A discrete regularization operator L, which approximates the Laplacian, is used to penalize solutions with large second derivatives.

It is dangerous to apply the finite-difference operator L to angles, because they are defined modulo 360°. Let us consider for example two angles $\phi_1 = 1^\circ$ and $\phi_2 = -1^\circ$. The difference between the two angles is $\phi_1 - \phi_2 = 2^\circ$ but had we defined $\phi_2 = 359^\circ$ then the difference would be $\phi_1 - \phi_2 = -358^\circ$. To avoid this problem, we construct the pseudo-vector $\boldsymbol{\Gamma}$ from the parameters γ, θ and ϕ inside block I:

$$\boldsymbol{\Gamma}_I = \begin{pmatrix} \gamma_I \cos\phi_I \sin\theta_I \\ \gamma_I \sin\phi_I \sin\theta_I \\ \gamma_I \cos\theta_I \end{pmatrix}, \tag{54}$$

and apply the Laplacian operator to this new combination of parameters. For example, the 2-D Laplacian operator in the vertical plane (x, z) applied on block (i, j) is defined by

$$\mathrm{L}(\Gamma_{i,j}) = \Gamma_{i-1,j} + \Gamma_{i+1,j} + \Gamma_{i,j-1} + \Gamma_{i,j+1} - 4\,\Gamma_{i,j}, \tag{55}$$

where i and j are the horizontal and vertical block indices. Generalizing this definition to three dimensions is straightforward. Introducing the matrix $\mathbf{R}$ containing the partial derivatives of the Laplacian operator with respect to model parameters

$$\mathbf{R} = \left(\frac{\partial \mathbf{L}}{\partial \mathbf{m}} \right)_{\mathbf{m}_n}, \tag{56}$$

leads us to the minimum of the regularized misfit function:

$$\chi(\mathbf{\Delta m}) = [\mathbf{S}(\mathbf{m}_n) + \mathbf{G}\mathbf{\Delta m} - \mathbf{S}_{\rm obs}]^t\, \mathbf{C}_{\rm S}^{-1}\, [\mathbf{S}(\mathbf{m}_n) + \mathbf{G}\mathbf{\Delta m} - \mathbf{S}_{\rm obs}]$$
$$+ [\mathbf{m}_n + \mathbf{\Delta m} - \mathbf{m}_{\rm prior}]^t\, \mathbf{C}_{\rm M}^{-1}\, [\mathbf{m}_n + \mathbf{\Delta m} - \mathbf{m}_{\rm prior}] \quad (57)$$

$$+\lambda^2 [\mathrm{L}(\mathbf{m}_n) + \mathbf{R}\mathbf{\Delta m}]^t\, [\mathrm{L}(\mathbf{m}_n) + \mathbf{R}\mathbf{\Delta m}] \quad (58)$$

where λ is a smoothness coefficient. The model perturbations are then solutions of the linear system

$$\left(\mathbf{G}^t\mathbf{C}_{\rm S}^{-1}\mathbf{G} + \mathbf{C}_{\rm M}^{-1} + \lambda^2\mathbf{R}^t\mathbf{R}\right)\mathbf{\Delta m} = \mathbf{G}^t\mathbf{C}_{\rm S}^{-1}[\mathbf{S}_{\rm obs} - \mathbf{S}(\mathbf{m}_n)] + \mathbf{C}_{\rm M}^{-1}[\mathbf{m}_{\rm prior} - \mathbf{m_n}] - \lambda^2\mathbf{R}^t\mathrm{L}(\mathbf{m}_n). \quad (59)$$

6.5 Resolution of the inverse problem

The linear system (59) is solved by LSQR (Paige & Saunders 1982; Nolet 1987), and the model is updated by the model perturbations $\mathbf{\Delta m}$:

$$\mathbf{m}_{n+1} = \mathbf{m}_n + \mu\mathbf{\Delta m}, \quad (60)$$

where the optimal value of μ giving the largest misfit reduction is found by linear search. The process is repeated until the misfit function stops decreasing.

7 A 2-D EXAMPLE

The synthetic test is designed to illustrate two important properties of finite-frequency vectorial tomography. First, the whole method relies on finite-frequency effects, not described by ray theory. To emphasize this point, we assume that *SKS* waves propagate vertically and introduce some radial heterogeneity in the input model. Thus, all the rays are parallel and ray theory would offer no depth resolution. In contrast, it will be shown that finite-frequency tomography retrieves the anisotropic anomalies at the correct depths. Second, finite-frequency tomography allows us to image heterogeneities smaller than the size of the Fresnel zone. To illustrate this last property, we will introduce both lateral and vertical variations of anisotropy over distances smaller than the size of the Fresnel zone, and show that we can recover them by finite-frequency tomography.

Note that the goal of the synthetic inversion test is not to estimate spatial resolution. Spatial resolution will depend on the azimuthal distribution of *SKS* waves, the geometry of the array, and the quality and number of *SKS* records. This issue will be addressed in a subsequent study applying on a specific real data set.

7.1 Description of the model and of the recording array

The model is composed of an homogeneous anisotropic layer with 6 per cent anisotropy ($\gamma = -0.06$), from 50 to 150 km depth. The fast symmetry axis lies in the horizontal plane ($\theta = 90^\circ$), along the N–S direction ($\phi = 0^\circ$) everywhere in the anisotropic layer except between $x = -50$ km and $x = +50$ km where the fast axis azimuth has a sinusoidal variation with an amplitude of 30° and a wavelength of 100 km in the horizontal and vertical directions. The input anisotropic model is shown in Fig. 4. For a vertical propagation of shear waves and a symmetry axis oriented in the horizontal plane, the anisotropic parameter η has no contribution. To further reduce the number of parameters, we assume that the anisotropic medium is invariant along the y direction. The recording array is composed of 11 stations, positioned every 20 km from -100 km to $+100$ km along the surface.

7.2 The synthetic data set

Synthetic splitting intensity is computed by calculating the volume integrals (42) in the fine 2 km grid, for nine different polarizations of the incoming vertical *SKS* waves. The complete data set is thus composed of 99 splitting intensities. The azimuthal coverage is rather poor, and should be comparable to that expected in a real case. The splitting intensities for the stations located at $x = 100$ km (solid circles) and at $x = 0$ km (empty squares) are shown in Fig. 5. We observe that for a vertically propagating *SKS* wave, splitting intensity has a sinusoidal variation with the polarization of the *SKS* wave, as already shown in Favier & Chevrot (2003). The apparent fast direction is the same at both stations, and the only indication of the presence of anisotropic heterogeneities under the array comes from the spatial variations in the amplitude of splitting intensity.

7.3 *A priori* information

The model is discretized with 10 km square blocks, between 30 and 200 km depth. Inside each block, anisotropy is parametrized by ϕ, the azimuth of the symmetry axis in the horizontal plane, and γ, the amplitude of shear wave anisotropy. We assume that the amplitude of anisotropy is known *a priori*, and set $\gamma_{\rm prior} = -0.06$, with a standard deviation of 0.03. The last choice involves setting the smoothness

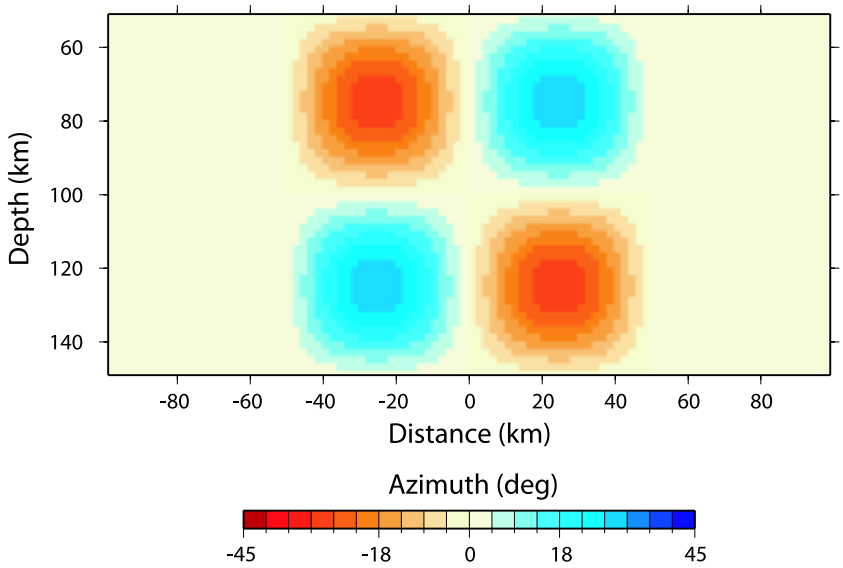

Figure 4. Input pattern of ϕ, the fast axis azimuth in the horizontal plane. The input pattern for γ, not shown, is $\gamma = -0.06$ between 50 and 150 km depth.

coefficient λ. Using values that are too small will give too rough models, while using values that are too large will result in a poor fit to the data.

7.4 Results

Starting from the initial model described in the previous section, minimizing the misfit function did not produce a good fit to the data. The reason is that assuming an incorrect depth interval for anisotropy introduced spurious features into the solution. To solve this problem, it was necessary to add the depth of the bottom and top of the anisotropic layer as additional free parameters. The partial derivatives of $\mathbf{S}$ with respect to z_1, the depth of the bottom of the anisotropic layer, and z_2, the depth of the top of the anisotropic layer are given by

$$\frac{\partial \mathbf{S}}{\partial z_1} = \frac{1}{\Delta z_1} \int_{z_1+\Delta z_1}^{z_1} dz \int_{-\infty}^{+\infty} \int_{-\infty}^{+\infty} K_\gamma(x, y, z)\, dx\, dy, \tag{61}$$

$$\frac{\partial \mathbf{S}}{\partial z_2} = \frac{1}{\Delta z_2} \int_{z_2}^{z_2+\Delta z_2} dz \int_{-\infty}^{+\infty} \int_{-\infty}^{+\infty} K_\gamma(x, y, z)\, dx\, dy. \tag{62}$$

The correct values of z_1 and z_2 were found after the first iteration and convergence was then achieved after four iterations.

The final model is shown in Fig. 6. Both the location and amplitude of the variations of the symmetry axis orientations are correctly retrieved. The amplitude of anisotropy, described by γ, is also well recovered everywhere in the depth interval corresponding to the anisotropic layer.

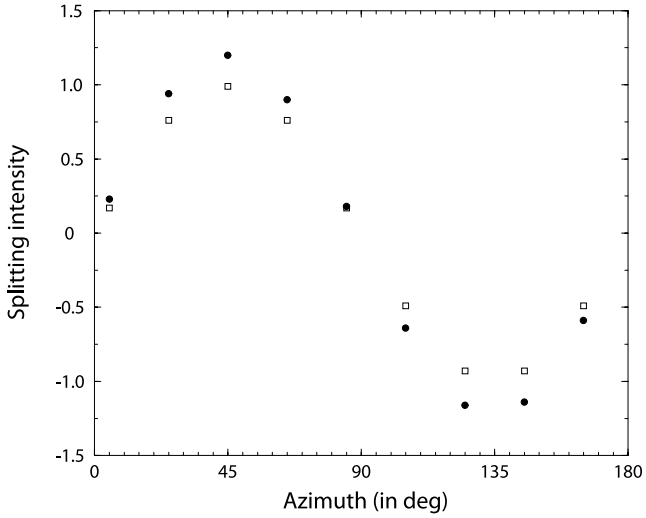

Figure 5. Synthetic splitting intensity data for the stations at the middle (squares) and at the end of the array (circles).

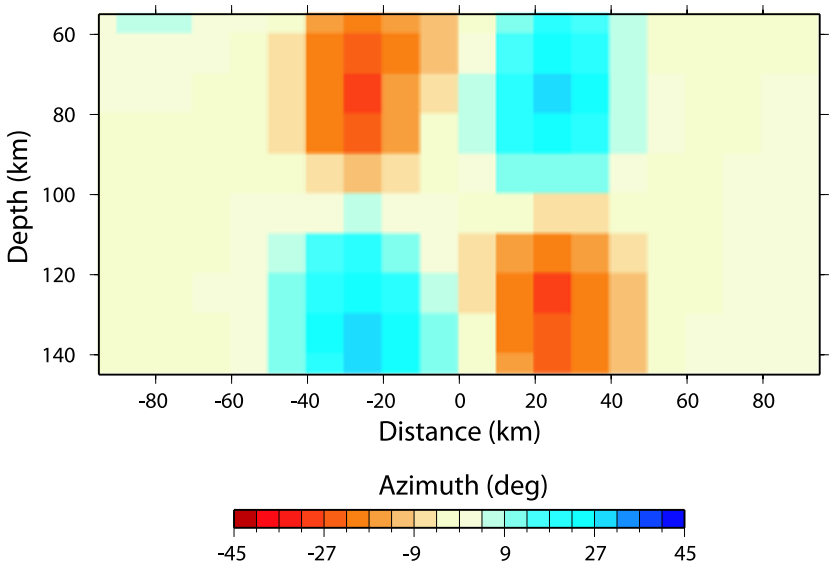

Figure 6. Output pattern of ϕ, the fast axis azimuth in the horizontal plane, in the noise-free case. The output pattern of γ is close to $\gamma = -0.06$ everywhere between 50 and 150 km depth (not shown).

7.5 Inversion of noisy data

The initial inversion test was performed in the absence of noise. A second experiment was conducted after adding normally distributed noise with a standard deviation of 0.1 to the synthetic data. In this case, special care has to be taken in the selection of the smoothing coefficient λ. The chosen value is the largest one that gives an acceptable misfit. Final data misfit as a function of model roughness $||\mathrm{L}\,(\mathbf{m})||^2$, for different values of the roughness parameter, is shown in Fig. 7. The curve has a typical L shape (Hansen 1992). The corner of this curve gives the best balance between data misfit and model norm. The model obtained with $\lambda = 50$ is shown in Fig. 8. The depth localization of the anisotropic heterogeneities is not as good as in the noise-free case, but the azimuthal pattern of the symmetry axis is still recovered.

8 DISCUSSION

Heterogeneous anisotropy may have subtle expressions in shear wave splitting measurements. In the synthetic case, small variations ~0.2 s of the apparent delay time in the absence of apparent variations of the fast direction could indeed be mistakenly interpreted as evidence of homogeneous anisotropy in the underlying medium. Similar observations were made in southern California, where the apparent fast direction is predominantly E-W, but where the delay times show significant variations over distances less than 100 km (e.g. Polet & Kanamori 2002). These variations could be related to short wavelength variations in anisotropy, for example to strong anisotropy localized in lithospheric-scale

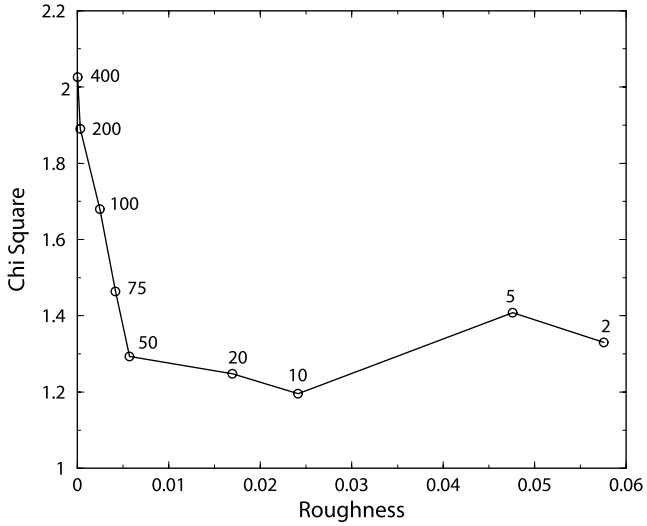

Figure 7. χ^2 data misfit versus model roughness for different values of the smoothness coefficient λ.

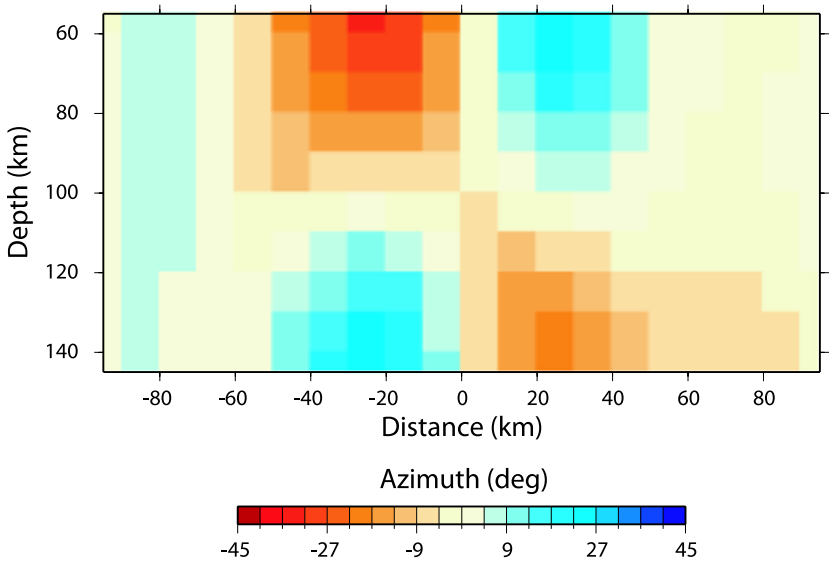

Figure 8. Output pattern of ϕ, the fast axis azimuth in the horizontal plane, in the case where Gaussian random noise with a standard deviation of 0.1 has been added to the synthetic data. The value of the roughness parameter is $\lambda = 50$. The output pattern of γ is close to $\gamma = -0.06$ everywhere between 50 and 150 km depth (not shown).

shear zones. This possibility, which has important implications for the deformation and rheology of the lithosphere, should be investigated in future studies.

That the algorithm retains its ability to retrieve the correct anisotropic pattern in a case where the noise level compares to the variations of splitting intensity produced by anisotropic heterogeneities may be surprising at first sight. However, because the splitting variation of anisotropy is sinusoidal, the only requirement for the inversion to be successful is that the sinusoidal pattern of the model represents the true sinusoidal variation of splitting intensity. In other words, errors in individual splitting measurements are averaged over the whole azimuthal range, and the error on apparent splitting parameters at a particular station decreases as $\sqrt{n}$, with n the number of *SKS* wave azimuths available at a particular station. Hence, this method is very robust, and is relatively insensitive to even large random errors in individual splitting measurements.

The moderate density of the array and relatively small azimuthal coverage used in the numerical tests were found sufficient to image seismic anisotropy. It would be easy to improve spatial resolution by measuring splitting intensity on each *SKS* record in different frequency bands. Therefore, we may be optimistic about using this approach successfully on real data.

In this study, the reference isotropic medium was assumed to be homogeneous, making the computation of the sensitivity kernels very efficient. It would be easy to generalize this theory to the case of a spherically symmetric isotropic reference medium or to a 3-D isotropic reference medium. Because shear wave splitting is to first-order insensitive to isotropic heterogeneities, they should have a limited influence on the inversion results. A key ingredient in any computation is the near field, which is necessary to correctly describe the sensitivity in the uppermost mantle, owing to the low frequency content of *SKS* waves (Favier *et al.* 2004). Another straightforward development would be to generalize the theory to orthorhombic anisotropy, though it is doubtful that seismologists will ever be able to constrain the large number of additional parameters which are necessary to describe this symmetry from seismological data alone. The coordinate-free representation of orthorhombic media necessary to derive the Fréchet kernels is given in Appendix A. Formulae that may be useful to compute sensitivity kernels in radially anisotropic media (hexagonal symmetry with a vertical symmetry axis) are given in Appendix C.

9 CONCLUSIONS

The splitting intensity, which measures the amplitude of the transverse component of *SKS* waves, is a very convenient seismological observable to image seismic anisotropy. Assuming transverse isotropy, one can formulate a non-linear inverse problem where the unknowns are two anisotropic parameters γ and η, and two angles describing the orientation of the symmetry axis at each point of the medium. Analytic expressions for sensitivity kernels that relate splitting intensity to perturbations of the elastic parameters and orientation of the symmetry axis in transversely isotropic media have been derived. These kernels have been validated by comparison with a resolution of the wave equation based upon a SEM. A synthetic 2-D test on a noisy data set has shown that anisotropic heterogeneities smaller than the wavelength can be retrieved, with excellent resolution in both lateral and vertical dimensions. Using a dense array of broad-band stations, we should thus be able to image the small-scale, 3-D anisotropic structure of the upper mantle. Application of this new imaging technique to a real data set will be presented in a forthcoming publication.

ACKNOWLEDGMENTS

This research was supported by the INSU program 'DyETI'. Thanks to Dimitri Komatitsch for his help in the implementation of the SEM code and Noémie Favier and Marie Calvet for helpful discussions. Kurt Feigl helped prune the dangling participles. Reviews by F. A. Dahlen and V. Maupin, and comments of the associate editors T. W. Becker and J. Virieux improved the clarity of the final manuscript.

REFERENCES

Aki, K. & Richards, P.G., 1980, *Quantitative Seismology, Theory and Methods,* Vol. 1, 2, Freeman, New York.

Backus, G.E., 1970, A geometrical picture of anisotropic tensor, *Rev. Geophys. Space Phys.,* **8,** 633–671.

Becker, T.W., Chevrot, S., Schulte-Pelkum, V. & Blackman, D.K., 2006, Statistical properties of seismic anisotropy in the upper mantle explored by geodynamic models, *J. geophys. Res.*, submitted.

Browaeys, J. & Chevrot, S., 2004, Decomposition of the elastic tensor and geophysical applications, *Geophys. J. Int.,* **159,** 667–678.

Chevrot, S., 2000, Multichannel analysis of shear wave splitting, *J. geophys. Res.,* **105,** 21 579–21 590.

Chevrot, S. & van der Hilst, R., 2003, On the effects of a dipping symmetry axis on shear wave splitting measurements in a transversely isotropic medium, *Geophys. J. Int.,* **152,** 497–505.

Chevrot, S., Favier, N. & Komatitsch, D., 2004, Shear wave splitting in three-dimensional anisotropic media, *Geophys. J. Int.,* **159,** 711–720.

Dahlen, F.A., Hung, S.H. & Nolet, G., 2000, Fréchet kernels for finite-frequency traveltimes—I. Theory, *Geophys. J. Int.,* **141,** 157–174.

Favier, N. & Chevrot, S., 2003, Sensitivity kernels for shear wave splitting in transverse isotropic media, *Geophys. J. Int.,* **153,** 213–228.

Favier, N., Chevrot, S. & Komatitsch, D., 2004, Near-field influences on shear wave splitting and traveltime sensitivity kernels, *Geophys. J. Int.,* **156,** 467–482.

Fouch, M.J., Fischer, K.M. & Parmentier, E.M., 2000, Shear wave splitting, continental keels, and patterns of mantle flow, *J. geophys. Res.,* **105,** 6255–6275.

Fouch, M.J., Silver, P.G., Bell, D.R. & Lee, J.N., 2004, Small-scale variations in seismic anisotropy near Kimberley South Africa, *Geophys. J. Int.,* **157,** 764–774.

Gangi, A.F., 2000, Fourth-order elastic-moduli tensors by inspection, in *Proceedings of the Ninth International Workshop on Seismic Anisotropy*, *SEG*.

Gradshteyn, I. & Ryzhik, I., 1965, *Table of Integrals, Series, and Products,* Academic Press, New York.

Grésillaud, A. & Cara, M., 1996, Anisotropy and P-wave tomography: a new approach for inverting teleseismic data from a dense array of stations, *Geophys. J. Int.,* **126,** 77–91.

Hansen, P.C., 1992, Analysis of discrete ill-posed problems by means of the L-curve, *SIAM Rev.,* **34,** 561–580.

Helbig, K., 1994, *Foundations of anisotropy for exploration seismics,* Pergamon.

Herquel, G., Tapponnier, P., Wittliger, G., Mei, J. & Danian, S., 1999, Teleseismic shear wave splitting and lithospheric anisotropy beneath and across the Altyn Tagh fault, *Geophys. Res. Lett.,* **26,** 3225–3228.

Houseman, G.A. & England, P.C., 1986, Finite strain calculations of continental deformation 1. Method and general results of convergence zones, *J. geophys. Res.,* **91,** 3651–3663.

Hudson, J.A., 1977, Scattered waves in the coda of P, *J. geophys. Res.,* **43,** 359–374.

Jech, J. & Pšenčík, I., 1989, First-order perturbation method for anisotropic media, *Geophys. J. Int.,* **99,** 369–376.

Jeffreys, H., 1931, *Cartesian tensors,* Cambridge University Press, London.

Kaminski, E. & Ribe, N.M., 2001, A kinematic model for recrystallization and texture development in olivine polycrystals, *Earth planet. Sci. Lett.,* **189,** 253–267.

Komatitsch, D. & Tromp, J., 2002, Spectral-element simulations of global seismic wave propagation-I. Validation, *Geophys. J. Int,* **149,** 390–412.

Komatitsch, D., Barnes, C. & Tromp, J., 2000, Simulation of anisotropic wave propagation based upon a spectral element method, *Geophysics,* **65**(4), 1251–1260.

Mensch, T. & Farra, V., 2002, P-wave tomography in inhomogeneous orthorhombic media, *Pure appl. Geophys.,* **159,** 1855–1879.

Mensch, T. & Rasolofosaon, P., 1997, Elastic-wave velocities in anisotropic media of arbitrary symmetry—generalization of Thomsen's parameters ϵ, δ and γ, *Geophys. J. Int.,* **128,** 43–64.

Montagner, J. & Tanimoto, T., 1991, Global upper mantle tomography of seismic velocities and anisotropies, *J. geophys. Res.,* **96,** 20 337–20 351.

Montagner, J.P. & Nataf, H.C., 1988, Vectorial tomography—I. Theory, *Geophys. J.*, **94,** 295–307.

Nolet, G., 1987, *Seismic tomography, with applications in global seismology and exploration geophysics,* chap. Seismic wave propagation and seismic tomography, ed. Nolet, G., pp. 1–23, D. Reidel Publishing Company.

Ory, J. & Pratt, R.G., 1995, Are our parameter estimators biased? The significance of finite-difference regularization operators, *Inv. Prob.,* **11,** 397–424.

Paige, C.C. & Saunders, M.A., 1982, LSQR: An algorithm for sparse linear equations and sparse least squares, *ACM Trans. Math. Softw.,* **8,** 43–71.

Polet, J. & Kanamori, H., 2002, Anisotropy beneath California: shear wave splitting measurements using a dense array, *Geophys. J. Int.,* **149,** 314–328.

Pratt, R.G. & Chapman, C.H., 1992, Traveltime tomography in anisotropic media–II. Application, *Geophys. J. Int.,* **109,** 20–37.

Saltzer, R.L., Gaherty, J.B. & Jordan, T.H., 2000, How are shear wave splitting measurements affected by variations in the orientation of azimuthal anisotropy with depth?, *Geophys. J. Int.,* **141,** 374–390.

Savage, M.K. & Silver, P.G., 1993, Mantle deformation and tectonics: Constraints from seismic anisotropy in the western United States, *Phys. Earth planet. Inter.,* **78,** 207–227.

Scales, J.A., Docherty, P. & Gersztenkorn, A., 1990, Regularisation of nonlinear inverse problems: imaging the near-surface weathering layer, *Inv. Prob.,* **6,** 115–131.

Silver, P.G., 1996, Seismic anisotropy beneath the continents: probing the depths of geology, *Annu. Rev. Earth Planet. Sci.,* **24,** 385–432.

Sobolev, S.V., Grésillaud, A. & Cara, M., 1999, How robust is isotropic delay time tomography for anisotropic mantle?, *Geophys. Res. Lett.,* **26,** 509–512.

Spies, M., 1994, Elastic waves in homogeneous and layered transversely isotropic media: plane waves and Gaussian wave packets. A general approach, *J. acoust. Soc. Am.,* **95,** 1748–1760.

Tapponnier, P., Peltzer, G., Dain, A.Y.L., Armijo, R. & Cobbold, P., 1982, Propagating extrusion tectonics in Asia: New insights from simple experiments with plasticine, *Geology,* **10,** 611–616.

Tarantola, A., 1987, *Inverse problem theory*, Elsevier, Amsterdam.

Červený, V. & Simoes-Filho, I.A., 1991, The traveltime perturbations for seismic body waves in factorized anisotropic inhomogeneous media, *Geophys. J. Int.,* **107,** 219–229.

Vinnik, L., Makeyeva, L.I., Milev, A. & Usenko, Y., 1992, Global patterns of azimuthal anisotropy and deformations in the continental mantle, *Geophys. J. Int.,* **111,** 433–447.

Vinnik, L., Bréger, L. & Romanowicz, B., 1998, Anisotropic structures at the base of the Earth's mantle, *Nature,* **393,** 564–567.

Zhang, S. & Karato, S.I., 1995, Lattice preferred orientation of olivine aggregates in simple shear, *Nature,* **375,** 774–777.

Zhang, S., Karato, S.I., Gerald, J.F., Faul, U.H. & Zhou, Y., 2000, Simple shear deformation of olivine aggregates, *Tectonophysics,* **316,** 133–152.

APPENDIX A: COORDINATE-FREE REPRESENTATION OF STIFFNESS TENSORS

A1 Isotropy

The elasticity tensor for an isotropic medium must contain only fourth-order tensors that are invariant under any rotation. The only fourth-order tensors that satisfy this condition are the fourth-order identity tensors (e.g. Jeffreys 1931). Therefore, the isotropic elasticity tensor is given by

$$c_{ijkl} = \lambda\, \delta_{ij}\delta_{kl} + \mu(\delta_{ik}\delta_{jl} + \delta_{il}\delta_{jk}), \tag{A1}$$

where the Lamé parameters λ and μ are related to the elastic parameters through the relations:

$$C_{11} = C_{22} = C_{33} = \lambda + 2\mu, \tag{A2}$$

$$C_{12} = C_{13} = C_{23} = \lambda, \tag{A3}$$

$$C_{44} = C_{55} = C_{66} = \mu. \tag{A4}$$

All the other components are null.

A2 Transverse isotropy

Transversely isotropic media have a single symmetry axis, defined here as the unit vector $\hat{\mathbf{s}}$. The coordinate-free expression of a transversely isotropic stiffness tensor is given by a sum of fourth-order tensors that are invariant under rotation around $\hat{\mathbf{s}}$ (Spies 1994):

$$\begin{aligned} c_{ijkl} = {} & (C_{11} - 2C_{66})\,\delta_{ij}\delta_{kl} + C_{66}(\delta_{ik}\delta_{jl} + \delta_{il}\delta_{jk}) \\ & + (C_{13} - C_{11} + 2C_{66})(\delta_{ij}s_k s_l + \delta_{kl}s_i s_j) \\ & + (C_{44} - C_{66})(\delta_{ik}s_j s_l + \delta_{il}s_j s_k + \delta_{jk}s_i s_l + \delta_{jl}s_i s_k) \\ & + (C_{11} + C_{33} - 2C_{13} - 4C_{44})s_i s_j s_k s_l \end{aligned} \tag{A5}$$

A3 Orthorhombic symmetry

Orthorhombic media possess three planes of symmetry that are mutually orthogonal. Let us define $\hat{\mathbf{a}}$, $\hat{\mathbf{b}}$, and $\hat{\mathbf{c}}$, the normals to the three mirror symmetry planes, which form an orthonormal system of coordinates. The coordinate-free expression of an orthorhombic stiffness tensor is given by:

$$\begin{aligned} c_{ijkl} = {} & (C_{13} + C_{23} - C_{12})\,\delta_{ij}\delta_{kl} + (C_{55} - C_{66} + C_{44})(\delta_{ik}\delta_{jl} + \delta_{il}\delta_{jk}) \\ & + (C_{12} - C_{23})(a_i a_j \delta_{kl} + \delta_{ij} a_k a_l) + (C_{12} - C_{13})(b_i b_j \delta_{kl} + \delta_{ij} b_k b_l) \\ & + (C_{66} - C_{44})(a_i a_k \delta_{jl} + a_i a_l \delta_{jk} + a_j a_l \delta_{ik} + a_j a_k \delta_{il}) \\ & + (C_{66} - C_{55})(b_i b_k \delta_{jl} + b_i b_l \delta_{jk} + b_j b_l \delta_{ik} + b_j b_k \delta_{il}) \\ & + (C_{11} - C_{13} + C_{23} - C_{12} + 2C_{44} - 2C_{55} - 2C_{66})\, a_i a_j a_k a_l \\ & + (C_{22} + C_{13} - C_{23} - C_{12} - 2C_{44} + 2C_{55} - 2C_{66})\, b_i b_j b_k b_l \\ & + (C_{33} - C_{13} - C_{23} + C_{12} - 2C_{44} - 2C_{55} + 2C_{66})\, c_i c_j c_k c_l \end{aligned} \tag{A6}$$

APPENDIX B: ANALYTICAL COMPUTATION OF THE FREQUENCY INTEGRALS

When the propagating pulse is the nth derivative of a Gaussian, the frequency integrals in (45) have simple analytical expressions. The integrals in the numerators can be computed from the relations (Gradshteyn & Ryzhik 1965):

$$\int x^{2n} e^{-b^2x^2} \cos ax\; dx = (-1)^n \frac{\sqrt{\pi}}{(2b)^{2n+1}} \exp\left(-\frac{a^2}{4b^2}\right) H_{2n}\left(\frac{a}{2b}\right), \tag{B1}$$

$$\int x^{2n+1} e^{-b^2x^2} \sin ax\; dx = (-1)^n \frac{\sqrt{\pi}}{(2b)^{2n+2}} \exp\left(-\frac{a^2}{4b^2}\right) H_{2n+1}\left(\frac{a}{2b}\right), \tag{B2}$$

where H_n is the nth order Hermite polynomial, and the denominators from (Gradshteyn & Ryzhik 1965):

$$\int x^{2n} e^{-b^2x^2}\; dx = \frac{(2n-1)!!\sqrt{\pi}}{2(2b^2)^n b}, \tag{B3}$$

where $(2n-1)!!$ denotes the factorial product of odd numbers up to $2n-1$.

APPENDIX C: RADIAL ANISOTROPY

Radial anisotropy, the particular case of transverse isotropy with a vertical symmetry axis, is of interest to describe anisotropy in some regions of the deep earth such as the D' layer (e.g. Vinnik *et al.* 1998). In this particular case, we can use eq. (20) to calculate the scattering coefficients for P, SV and SH.

For *P* waves, we get:

$$\Omega_\alpha = 2, \tag{C1}$$

$$\Omega_\epsilon = 2\left[(\hat{\mathbf{p}}'\cdot\hat{\mathbf{s}})^2(\hat{\mathbf{p}}\cdot\hat{\mathbf{s}})^2 - (\hat{\mathbf{p}}'\cdot\hat{\mathbf{s}})^2 - (\hat{\mathbf{p}}\cdot\hat{\mathbf{s}})^2\right], \tag{C2}$$

$$\Omega_\delta = (\hat{\mathbf{p}}'\cdot\hat{\mathbf{s}})^2 + (\hat{\mathbf{p}}\cdot\hat{\mathbf{s}})^2 - 2(\hat{\mathbf{p}}'\cdot\hat{\mathbf{s}})^2(\hat{\mathbf{p}}\cdot\hat{\mathbf{s}})^2, \tag{C3}$$

$$\Omega_\gamma = 4\left[(\hat{\mathbf{p}}'\cdot\hat{\mathbf{s}})^2 + (\hat{\mathbf{p}}\cdot\hat{\mathbf{s}})^2 - 2(\hat{\mathbf{p}}'\cdot\hat{\mathbf{p}})^2(\hat{\mathbf{p}}'\cdot\hat{\mathbf{s}})^2(\hat{\mathbf{p}}\cdot\hat{\mathbf{s}})^2\right], \tag{C4}$$

for *SV*, $(\hat{\mathbf{p}}'\cdot\hat{\mathbf{g}}') = 0$:

$$\Omega_\beta = 2\left[(\hat{\mathbf{p}}'\cdot\hat{\mathbf{p}})(\hat{\mathbf{g}}'\cdot\hat{\mathbf{g}}) + (\hat{\mathbf{g}}'\cdot\hat{\mathbf{p}})(\hat{\mathbf{p}}'\cdot\hat{\mathbf{g}})\right], \tag{C5}$$

$$\Omega_\epsilon = 2(\hat{\mathbf{p}}'\cdot\hat{\mathbf{s}})(\hat{\mathbf{p}}\cdot\hat{\mathbf{s}})(\hat{\mathbf{g}}'\cdot\hat{\mathbf{s}})(\hat{\mathbf{g}}\cdot\hat{\mathbf{s}}), \tag{C6}$$

$$\Omega_\delta = -2(\hat{\mathbf{p}}'\cdot\hat{\mathbf{s}})(\hat{\mathbf{p}}\cdot\hat{\mathbf{s}})(\hat{\mathbf{g}}'\cdot\hat{\mathbf{s}})(\hat{\mathbf{g}}\cdot\hat{\mathbf{s}}), \tag{C7}$$

$$\begin{aligned}\Omega_\gamma = {} & -2\{(\hat{\mathbf{g}}'\cdot\hat{\mathbf{s}})\left[(\hat{\mathbf{g}}\cdot\hat{\mathbf{s}})(\hat{\mathbf{p}}'\cdot\hat{\mathbf{p}}) + (\hat{\mathbf{p}}\cdot\hat{\mathbf{s}})(\hat{\mathbf{p}}'\cdot\hat{\mathbf{g}})\right] \\ & +(\hat{\mathbf{p}}'\cdot\hat{\mathbf{s}})\left[(\hat{\mathbf{g}}\cdot\hat{\mathbf{s}})(\hat{\mathbf{g}}'\cdot\hat{\mathbf{p}}) + (\hat{\mathbf{p}}\cdot\hat{\mathbf{s}})(\hat{\mathbf{g}}'\cdot\hat{\mathbf{g}})\right]\}\end{aligned} \tag{C8}$$

For SH, $(\hat{\mathbf{g}}'\cdot\hat{\mathbf{s}}) = (\hat{\mathbf{g}}\cdot\hat{\mathbf{s}}) = 0$, and:

$$\Omega_\beta = 2\left[(\hat{\mathbf{p}}'\cdot\hat{\mathbf{p}})(\hat{\mathbf{g}}'\cdot\hat{\mathbf{g}}) + (\hat{\mathbf{p}}'\cdot\hat{\mathbf{g}})(\hat{\mathbf{g}}'\cdot\hat{\mathbf{p}})\right], \tag{C9}$$

$$\Omega_\gamma = -2(\hat{\mathbf{p}}'\cdot\hat{\mathbf{s}})(\hat{\mathbf{p}}\cdot\hat{\mathbf{s}})(\hat{\mathbf{g}}'\cdot\hat{\mathbf{g}}). \tag{C10}$$

All the omitted coefficients are zero.